Coexistence of hcp and bct Phases during In Situ Superlattice Assembly from Faceted Colloidal Nanocrystals

Irina Lokteva[*†‡], Michael Koof[†‡], Michael Walther[†], Gerhard Grübel[†‡], and Felix Lehmkühler[†‡]*

[†] Deutsches Elektronen-Synchrotron (DESY), Notkestraße 85, 22607 Hamburg, Germany

[‡] The Hamburg Centre for Ultrafast Imaging (CUI), Luruper Chaussee 149, 22761 Hamburg, Germany

*E-mail: irina.lokteva@desy.de

ABSTRACT

We study the in situ self-assembly of faceted PbS nanocrystals from colloidal suspensions upon controlled solvent evaporation using time-resolved small-angle X-ray scattering and X-ray cross-correlation analysis. In our bulk-sensitive experiment in transmission geometry, the superlattice crystallization is observed in real time revealing a hexagonal closed-packed (hcp) structure followed by formation of a body-centered cubic (bcc) superlattice. The bcc superlattice undergoes continuous tetragonal distortion in the solvated state shortly after its formation, resulting in the body-centered tetragonal (bct) structure. Upon solvent evaporation, the bct superstructure becomes more pronounced with the still coexisting hcp phase. These findings corroborate the existing simulations of assembling cuboctahedral-shaped particles and illustrate that we observed the predicted equilibrium states. This work is essential for a deeper understanding of the fundamental forces that direct nanocrystal assembly including nanocrystal shape and ligand coverage.

TOC GRAPHICS

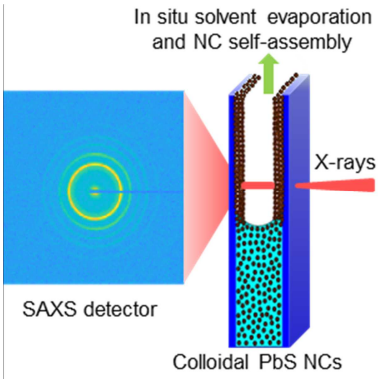

KEYWORDS. Small angle X-ray scattering (SAXS), X-ray cross correlation analysis (XCCA), evaporative induced self-assembly, lead sulfide (PbS), time-resolved superlattice crystallization.

Bottom-up fabrication of nanocrystal (NC) superlattices with novel electronic or optoelectronic properties requires thorough understanding of the mechanisms governing the NC assembly into a preferred superlattice phase. Despite a large number of studies available on NC supracrystallization[1-7] the challenge remains to unravel the assembly path due to intricate interplay of ligand–ligand and solvent–ligand interactions as well as anisotropy in the inorganic core and the surrounding ligand shell. In particular, for non-spherical polyhedral nanocrystals the selective facet-to-facet interactions induced by the anisotropic shape influence the assembly pathway leading to the intriguing packing structures of nanocrystal solids.[8,9] In that regard, in situ monitoring of the directed self-organization of colloidal faceted NCs into ordered superstructures helps to gain unique insights into the fundamental processes guiding the anisotropic assembly.

Recently, time-resolved X-ray scattering methods have been demonstrated to be a powerful tool for studying the NC assembly in real time under controlled experimental conditions.[10-20] The majority of these reports utilize the grazing-incidence small-angle X-ray scattering (GISAXS) technique for the in situ measurements of the self-assembly of colloidal NCs upon solvent evaporation.[11-15, 19] However, the GISAXS geometry is limited to the surface characterization due to small incident angles of the X-ray beam and cannot deliver information about bulk superlattice structure. In our previous studies,[21,22] we demonstrated in situ small-angle X-ray scattering (SAXS) measurements in transmission mode of the evaporative self-organization of colloidal NCs into superstructures with long range order. In this technique, the structural information on a thick nanocrystal solid can be monitored both in the solvated and dried states during the real-time in situ NC assembly.

Here, using in situ SAXS, we investigate the real-time assembly of faceted 7.8 nm PbS NCs passivated with oleic acid ligands into highly ordered superlattices during controlled solvent evaporation from heptane and toluene suspensions. For truncated lead chalcogenide NC superlattices, different assembly phases, such as e.g. face-centered cubic (fcc), body-centered cubic (bcc), and body-centered tetragonal (bct), detected either ex situ or in situ have been reported.[11,12,15,23-38] The origin of various observed superlattice structures and the different degree of ordering are believed to be caused by differences in NC size, shape, dispersity, composition, ligand length and ligand grafting density, NC concentration, assembly pathway (e.g., solvent evaporation or destabilization by antisolvent diffusion), cell/assembly geometry, rate of the assembly process, ligand–solvent and ligand–ligand interactions, or a combination thereof.[11,12,15,23-38]

In this study, we use a recently designed custom-made sample environment for in situ SAXS measurements in transmission mode described in detail in Ref. 21. In this chamber, the solvent in the colloidal suspension evaporates slowly (e.g., the evaporation rate is < 0.3 µl/min for heptane and < 0.2 µl/min for toluene) and the nanocrystals form highly ordered superlattices along the cell windows (Figure 1a). The start of the superlattice formation can be observed in SAXS patterns when the evaporation front line reaches the corresponding vertical position on the cell windows (Figure 1a).[21]

Representative transmission electron microscopy (TEM) and high-resolution TEM (HRTEM) images of PbS NCs used in this study are shown in Figures 1b and c, respectively. The HRTEM images (Figure 1c) confirm that the NCs exhibit pronounced faceting and can be approximated by a cuboctahedral shape in accordance with previous observations for similar sized lead chalcogenide nanocrystals.[15,33,39] The SAXS profile of a colloidal NC suspension in heptane can

be described using a spherical form factor for polydisperse hard spheres, which results in the nanocrystal radius of 3.92 nm with 10% dispersity (Figure 1d). This size is in good agreement with the size obtained from the UV-Vis-NIR absorption spectroscopy (Figure S1 and description in the Supporting Information). Using thermogravimetric analysis we estimated that the ligand grafting density of our oleic acid capped nanocrystals is 4.5 ligands/nm^2 (Figure S2 and calculations in the Supporting Information). It has to be noted that the degree of ligand coverage is an important parameter that influences the assembly outcome as it has been reported both in experimental and theoretical investigations.[1,3,40-42] In particular, for oleic acid capped lead chalcogenide NCs, there could be additional anisotropy in the ligand corona due to selective desorption of weakly bound ligand molecules from $\{100\}_{PbS}$ facets, which leads to different superlattice phases.[42]

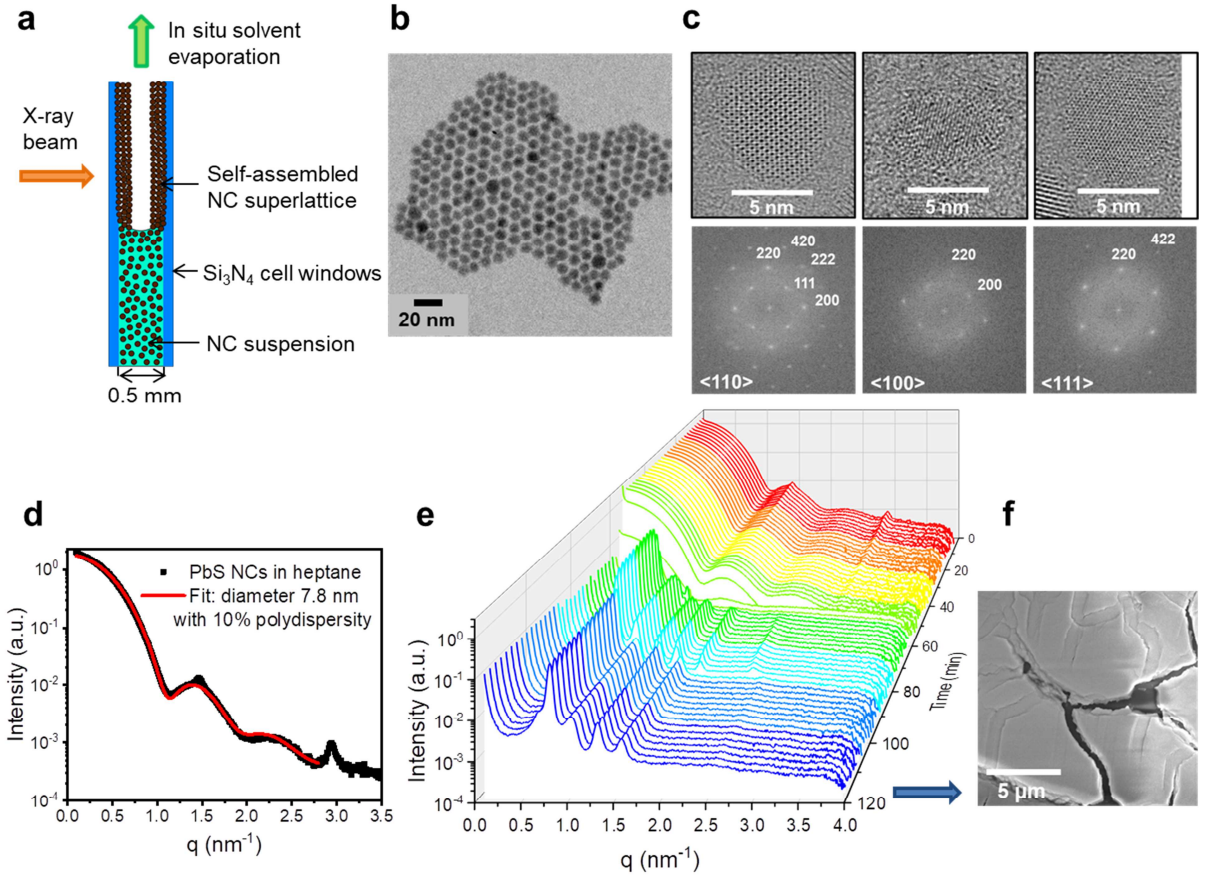

Figure 1. (a) Schematic representation of the sample cell used for the evaporation induced nanocrystal assembly for SAXS measurements in transmission mode. (b) TEM image of PbS nanocrystals used for the in situ self-assembly experiment. (c) Representative HRTEM images of PbS nanocrystals viewed along the <110>, <100>, and <111> directions with the corresponding Fourier transforms. (d) 1D SAXS curve of a 10 mg/ml colloidal suspension of PbS nanocrystals in heptane with a corresponding spherical form factor fit. The peaks at q = 1.47 and 2.94 nm^{-1} can be attributed to the crystalline oleic acid. (e) Time-resolved 1D SAXS curves recorded approximately every 2 min during the in situ self-assembly upon controlled solvent evaporation from a 10 mg/ml colloidal suspension of PbS nanocrystals in heptane. (f) Post-assembly SEM image of the nanocrystal superlattice film.

In our in situ experiment performed at beamline ID02 of the European Synchrotron Radiation Facility (ESRF),[43,44] the superlattice crystallization and transformation is observed in real time (Figure 1e). In the beginning of the self-assembly, the SAXS profiles show scattering arising from the form factor of the colloidal suspension (Figure 1d, e). Two peaks at scattering vector values of q_1 = 1.47 and q_2 = 2.94 nm^{-1} display a linear correlation of q_1/q_2 = 1 : 2 indicating the formation of a lamellar structure with an interlamellar spacing of $d_{(001)} \approx 4.3$ nm (Figure 1d). This lamellar ordering can be attributed to the crystalline oleic acid in accordance with previous observations, where the crystalline structure formed either by pure oleic acid molecules or by oleic acid ligands on nanoparticle surfaces was reported.[45,46,34] Rosenfeldt et al.[46] observed a similar sharp Bragg peak at q = 1.41 nm^{-1} (i.e., $d_{(001)} \approx 4.5$ nm) in the SAXS profile of a dilute suspension of oleic acid capped iron oxide nanocubes in toluene. Interestingly, the SAXS curve of spherical iron oxide nanoparticle suspensions did not exhibit such a peak. This suggests that

the lamellar structure of crystalline oleic acid molecules within the solvent is caused by the preferential orientation of faceted nanocrystals. During the assembly process, the initially observed lamellar packing structure in the colloidal suspension disappears with time indicating rearrangement of NCs and loss of the crystalline order between oleic acid molecules (Figure 1e). Upon slow solvent evaporation, nanocrystals form long-range ordered superlattices along cell windows evident by the appearance of the well-resolved diffraction peaks (Figure 1e). The post-assembly scanning electron microscopy (SEM) of dried superlattice films (Figure 1f) revealed that these films are 700–1000 nm thick, which confirms that the effects presented in this in situ transmission SAXS study describe the bulk NC assembly. The absolute time of the in situ assembly depends on the vertical position of the measurement point (Figure 1a) as well as the exact sample volume and amount of solvent used for the chamber saturation.[21,22] The data shown in this study were acquired at the measurement point located below the middle part of the silicon nitride windows, which is why the superlattice formation sets in after approximately 59 min of elapsed time. It has to be noted that other vertical points on the cell windows exhibit similar results as discussed throughout the paper. As demonstrated in our recent publication Ref. 21, the sample cell allows for monitoring the transitions of the superlattice structure in the swollen state, because the self-organized NC solid films in the upper part of the cell windows remain in the solvent vapor saturated atmosphere as long as the solvent is still present in the bulk suspension in the cell. The temporal point of the complete solvent evaporation can be precisely deduced from the simultaneous rearrangement of the superlattice structure at different vertical positions of the cell windows,[21] and thus the superlattice in the dried state can be characterized.

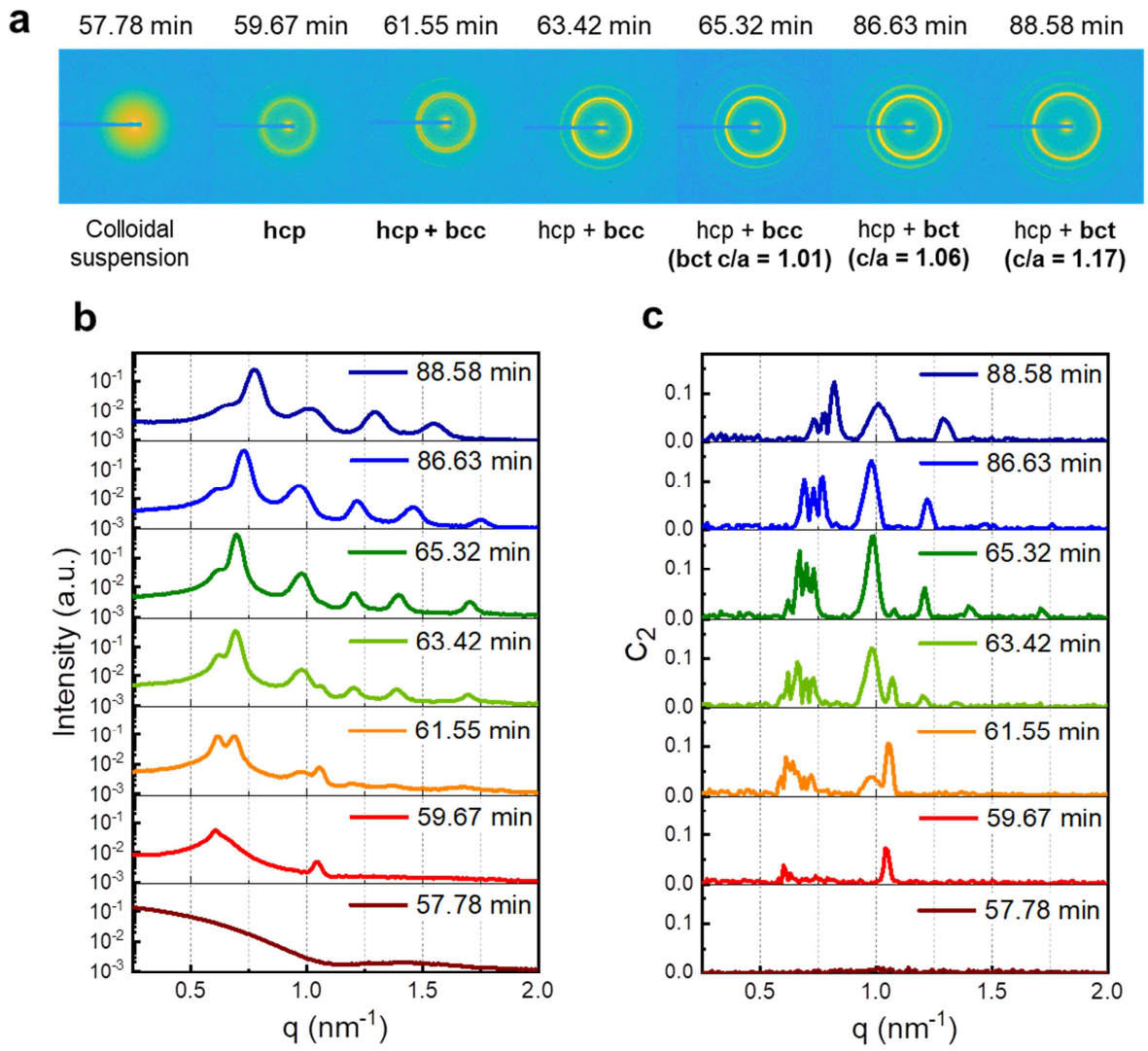

Figure 2. (a) 2D scattering patterns of a 10 mg/ml PbS NC suspension in heptane during controlled solvent evaporation. The obtained nanocrystal superlattice phases are indicated below the scattering patterns. The predominant structures observed at certain elapsed times after start of evaporation are shown in bold. More details for the superstructure lattice constants can be found in Figure S3. (b) 1D scattering curves obtained by azimuthal integration of 2D SAXS data shown in (a). These are the same curves depicted among others in Figure 1e. (c) The second Fourier coefficients C_2 of the cross-correlation function C calculated from 2D SAXS data shown in (a).

Figures 2a and b show representative two-dimensional SAXS patterns and the corresponding one-dimensional SAXS curves at different times of the self-assembly process. At 59.67 min of elapsed time after the start of evaporation, the superlattice is formed with Bragg peaks at q = 0.603 nm^{-1} and 1.046 nm^{-1}, which can be best described as the hexagonal closed-packed (hcp) structure (Figure 2a, b, Figure S3). The detailed evolution of the time-resolved SAXS curves with the corresponding fits of the superlattice crystallographic structure is shown in Figure S3 of the Supporting Information. At 61.55 min the hcp phase is accompanied by the bcc superlattice with the $(110)_{bcc}$ reflection at q = 0.688 nm^{-1}. The lattice constant of the newly formed bcc phase is 12.92 nm. After 63.42 min of evaporation, the bcc phase becomes more pronounced and dominates the hexagonal phase. At this point, the bcc superlattice exhibits a lattice constant of 12.85 nm. During the ongoing solvent evaporation, at 65.32 min of elapsed time the bcc superlattice starts to show a slight tetragonal distortion transforming into the bct phase, where the SAXS profile can be fitted by a bcc lattice with a = 12.8 nm or by a bct lattice with a = 12.75 nm and c = 12.87 nm (c/a = 1.01) due to the slight shift of the $(200)_{bcc}$ and $(220)_{bcc}$ reflections compared to the calculated values.

Subsequently, as the solvent continues to evaporate the tetragonal distortion becomes more pronounced and at 86.63 min the bct superlattice with lattice constants of a = 12.2 nm and c = 12.95 nm can be observed (Figure 2a, b, Figure S3). After the solvent has been evaporated completely at approximately 87.5 min of elapsed time, the superlattice rearranges into the bct structure with larger c/a ratio accompanied by broadening and disappearance of some Bragg reflections. Thus, at 88.58 min the bct superlattice exhibits lattice constants of a = 10.7 nm and c = 12.5 nm (Figure 2a, b, Figure S3). The obtained bct superlattice and the lattice constants in a dry bct superlattice are in line with previous observations, where the tetragonally distorted

superlattices of oleic acid capped PbS NCs were reported.[15,34-36] The nearest neighbor spacing in this bct structure, given by $NN_{bct} = \frac{\sqrt{(2a^2+c^2)}}{2}$, is 9.8 nm and the surface-to-surface separation distance between the nearest neighbor nanocrystals is $NN_{bct} - d_{NC} \approx 2$ nm. The second nearest neighbors are a distance of lattice constant a apart, so the gap between them is ≈ 2.9 nm. Novák et al.[35] attributed the origin of the bct phase in PbS NC superstructures to the fact that in the bct lattice ligands between both $\{100\}_{PbS}$–$\{100\}_{PbS}$ and $\{111\}_{PbS}$–$\{111\}_{PbS}$ facets can efficiently interact with each other stabilizing this structure compared to the symmetrical fcc and bcc lattices. This is in accordance with our observations where the interparticle distance between both the nearest neighbors and the second nearest neighbors is less than twice the fully extended length of the oleic acid molecule (2.29 nm)[40] suggesting that ligands strongly interact. Recent simulations have shown that despite common assumption that ligands interdigitate, the ligands between adjacent particles are more likely to splay out along the mid-plane between the cores[47] or bend and deflect away from each other[48], especially at high ligand densities.

In order to resolve the superlattice structure in detail, we performed the X-ray cross correlation analysis (XCCA),[49,50] which has been recently demonstrated to be a valuable tool to access structural information of crystalline materials beyond convectional pair correlation SAXS analysis.[36,51-55,22] The details of the XCCA method are described in Ref. 56. Briefly, this method is based on the evaluation of the angular cross-correlation function for each 2D diffraction pattern defined as $C(q,\Delta) = \frac{\langle I(q,\phi)I(q,\phi+\Delta)\rangle_\phi - \langle I(q,\phi)\rangle_\phi^2}{\langle I(q,\phi)\rangle_\phi^2}$, where ϕ is the azimuth angle of the 2D scattering pattern at fixed q and Δ is the correlation angle. Typically, Fourier coefficients of the cross-correlation function C(q, Δ) are analyzed to obtain measures of the symmetry of the diffraction pattern. Figure 2c shows the second Fourier coefficient C_2 of C as a function of q for

different evaporation times. These Fourier coefficients C_2 were calculated from scattering profiles shown in Figure 2a and are particularly sensitive to the symmetry of the diffraction patterns[57] and thus the presence of Bragg reflections in the scattering pattern according to Friedel's law. From comparison of SAXS curves in Figure 2b with Fourier coefficients C_2 in Figure 2c, it is evident that XCCA reveals hidden local symmetries in the scattering pattern. Thus, in Figure 2b at 63.42 min of elapsed time two broad peaks at q values of 0.62 and 0.695 nm^{-1}can be seen, whereas in Figure 2c at 63.42 min of elapsed time several sharp peaks can be observed at q values of 0.62, 0.66, 0.7, 0.73 nm^{-1}. The first three of the latter peaks can be attributed to the hcp phase with lattice constants of a = 11.8 nm and $c = \sqrt{8/3}\,a$ (for peak assignment see Figure S3). The hexagonal phase coexists even after complete solvent evaporation at 88.58 min of elapsed time with a = 9.9 nm and $c = \sqrt{8/3}\,a$, evident by three peaks at q = 0.73, 0.77 and 0.82 nm^{-1}, whereas the $(002)_{hcp}$ and $(101)_{hcp}$ peaks coincide with the $(101)_{bct}$ and $(110)_{bct}$ peaks, respectively (Figure 2c).

Figure 3a shows the whole time-resolved map of the Fourier coefficients C_2 values during the in situ self-assembly together with the fourth C_4 and the sixth C_6 Fourier coefficients of C as a function of the scattering vector q. The C_2 plot confirms the presence of three distinct peaks at q < 0.75 nm^{-1} in a swollen superlattice during real-time solvent evaporation and at q = 0.73, 0.77 and 0.82 nm^{-1} in a dried superlattice resulting from the hcp phase. Whereas Fourier coefficients C_2 indicate the symmetry of the diffraction pattern according to Friedel's law, Fourier coefficients C_4 and C_6 are sensitive to the four- and sixfold symmetry of the diffraction pattern, respectively, because in crystalline materials the cross-correlation function C exhibits maxima for Δ corresponding to angles between equivalent lattice planes.[51,52]

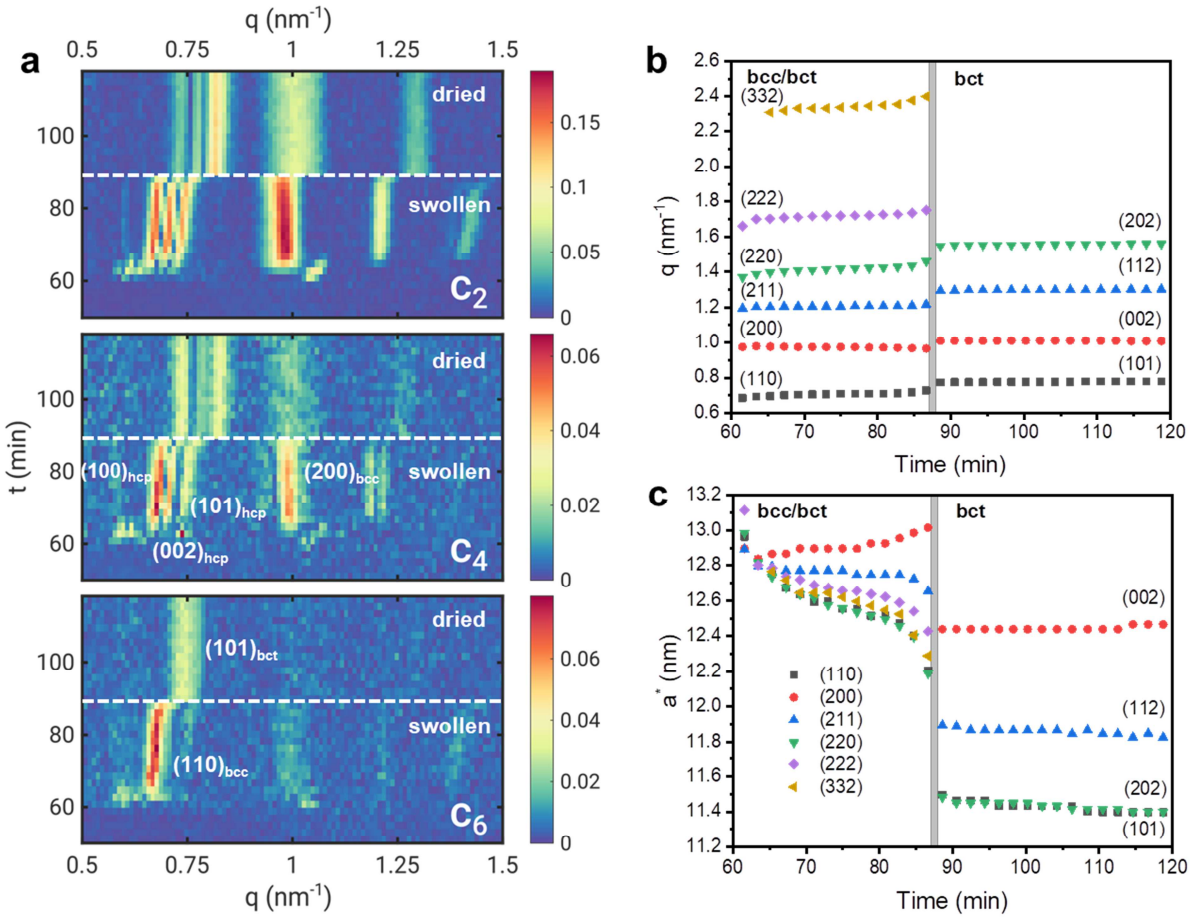

Figure 3. (a) Time-resolved second C_2, fourth C_4, and sixth C_6 Fourier coefficients of the cross-correlation function C calculated from scattering patterns during the in situ self-assembly experiment. The dotted line separates the swollen and dried superlattice states. Figure 2c shows the cuts of C_2 at chosen times from this plot. (b) Evolution of the Bragg peak positions with time for the bcc structure undergoing a tetragonal distortion in the solvated state and the resulting bct structure upon superlattice drying. The gray area depicts the moment of complete solvent evaporation. (c) Effective lattice constant a^* calculated from peak positions in (b). a^* represents the average value between lattice constants of a three-dimensional cell. For simplicity, only cubic phases are analyzed in (b) and (c).

For the $\{110\}_{bcc}$ and $\{101\}_{bct}$ reflections the angles between equivalent lattice planes are 60°, which is why the contributions to the Fourier coefficients C_6 (and not to the C_4) are expected, as discussed in our previous publication.[22] Analogously, the $\{200\}_{bcc}$ reflections with 90° between equivalent lattice planes contribute to the Fourier coefficients C_4. This is corroborated in Figure 3a. Additionally, the Fourier coefficients C_4 uncover three high intensity components at $q \leq 0.75$ nm^{-1}, which may result from the hcp phase because the cross-correlation function shows multiple peaks at the $\{100\}_{hcp}$, $\{002\}_{hcp}$, and $\{101\}_{hcp}$ reflections. These contributions to C_4 remain present in the dried superlattice as well with the anticipated shift of the peak positions upon superlattice shrinkage. Thus, the XCCA results clearly verify the phase coexistence both in the solvated and dried superstructures. Due to the contribution from crystallographic planes located in different crystallographic directions of the hcp phase, we can conclude that the observed hcp superlattice is three-dimensional.

The tetragonally distorted bcc nanocrystal superlattice exhibits continuous reduction in the *a*-axis upon slow solvent removal under the solvent vapor saturated environment, while the *c*-axis remains almost unchanged or shows a slight expansion. As it can be seen from the peak positions in Figure 3b, the tetragonal distortion of the bcc superlattice occurs through the $\{200\}_{bcc}$ and $\{211\}_{bcc}$ planes, because the distance between each of them does not undergo the expected reduction with time upon gradient solvent removal. The values of the effective lattice constant a^* (i.e. the average value of all three crystallographic directions) calculated from each of the Bragg reflections are presented in Figure 3c. Whereas the values resulting from the $\{110\}_{bcc}$, $\{220\}_{bcc}$, $\{222\}_{bcc}$, and $\{332\}_{bcc}$ reflections show expected reduction in the course of the assembly experiment, the effective lattice constant of the $\{211\}_{bcc}$ reflection exhibits a moderate decrease and the effective lattice constant of the $\{200\}_{bcc}$ reflection slowly expands (Figure 3c). Upon

complete drying at approximately 87.5 min of elapsed time, the bct structure becomes more pronounced with increase of the *c*/*a* ratio to about 1.17 compared to the *c*/*a* ratio of 1.06 in the solvated atmosphere (Figure 2a, Figure S3). The main lattice compression takes place along the *a*-axis (about 12% compared to the solvated state), whereas the *c*-axis compresses negligibly (about 3%).

Besides heptane as solvent, we have also studied the self-assembly of PbS NCs from a 10 mg/ml suspension in toluene because it has been reported that the nature of the ligand−solvent interactions may also play a role in the assembly process.[15,37,38,58] For toluene as solvent, the absolute time needed for the superlattice crystallization to set in was larger due to the lower vapor pressure of toluene at the same helium flow rate (Figure S4a). However, the self-assembly from toluene suspensions underwent exactly the same pathway resulting in the same superlattice phases and phase coexistence, as well as the same lattice parameters, even though the degree of ordering was slightly less, evident, e.g., by a smearing out of the $(002)_{bct}$ reflection after the solvent evaporation (Figure S4b). Similar mechanisms of the PbS NC self-organization from aliphatic heptane and aromatic toluene suspensions suggest that the system at the given experimental conditions reaches its equilibrium state.

Compared to the in situ GISAXS studies of the self-assembly of oleic acid capped PbS NCs from colloidal suspensions by Weidman et al.[12], where an fcc–bct–bcc superlattice transition was reported, we detect different assembly states in our in situ experiment, i.e. an hcp–bcc–bct transition. The hcp phase is observed at the earliest stages of superlattice crystallization followed by the growth of the bcc superstructure, which in turn immediately starts to show a tetragonal distortion caused by the gradual solvent removal. Upon drying, the bct phase becomes more pronounced, i.e. the *c*/*a* ratio increases to 1.17, and, surprisingly, the hcp phase continues to

coexist. The question arises as to why our experiment and that of Weidman et al.[12] reveal distinctly different superlattice states. The occurrence of the hcp superlattice is in accordance with our previous observations, where for the self-assemblies of 3.9 nm in diameter PbS NCs the hcp phase was recorded in the solvated superlattice state, which underwent transformation to the bcc superlattice upon complete solvent evaporation.[22] However, for the 7.8 nm sized PbS NCs the hcp phase coexists with the bct phase both in the solvated and dried states, which indicates a different mechanism of the superlattice assembly. 7.8 nm PbS NCs with a ligand-length-to-core-radius ratio of 0.58 are less soft compared to the 3.9 nm NCs, which is why the properties of the inorganic core determine the assembly outcome at a higher extent. Additionally, larger PbS NCs are known to exhibit highly pronounced faceting compared to smaller NCs, which is why the shape of the inorganic core and the surrounding ligand shell needs to be taken into account.

Patra et al.[48] recently used coarse-grained molecular dynamics simulations to calculate the ligand distribution around 7 nm PbS NCs functionalized with oleic acid at various ligand coverages. Their calculations showed that for ligand-rich nanoparticles, i.e. ligand grafting density > 3.6 nm^{-2}, the soft organic shell is uniformly thick around inorganic nanocrystal core. This implies that in our case, where the ligand grafting density is 4.5 nm^{-2} calculated considering a cuboctahedral shape of PbS NCs, the distribution of oleic acid molecules around a nanoparticle is uniform and ligands do not introduce additional anisotropy to the inorganic core. In this respect, the whole inorganic core – organic shell system used in this study can be considered to preserve cuboctahedral shape.

Gantapara et al.[59,60] have reported the thermodynamic equilibrium phase diagram of a family of truncated hard cubes at finite pressures using Monte Carlo simulations and free-energy calculations. The authors noted that at finite pressures the structures formed by self-assembly

differ substantially from the packings achieved at high pressures, i.e. under close-packed conditions.[8,9] According to Gantapara et al.,[59,60] for a cuboctahedron (shape parameter s = 0.5) the system undergoes a transition from a liquid through a phase coexistence region to the plastic hcp phase if $s < 0.5$ and to the plastic bct phase if $s > 0.5$. Plastic or rotator phases imply low orientational order of NCs, which is consistent with our data, where the complete Debye-Scherer rings are observed in the 2D wide-angle X-ray scattering (WAXS) patterns indicating various NC orientations (Figure S5). Time-resolved SAXS and WAXS data were acquired simultaneously as described in Ref. 21. In our experiment, we observe this coexistence of plastic hcp and bct phases which is predicted for s = 0.5. Moreover, the packing fraction of our oleic acid capped PbS NCs in the final bct superlattice at 88.58 min of elapsed time is 58% (for details see Supporting Information), which is in perfect agreement with the phase diagram of Gantapara et al.[59,60] This result indicates that our experiment, where a small amount of the colloidal suspension located in the confined environment between cell windows is evaporated in a solvent vapor saturated atmosphere at a very low evaporation rate, confirms the simulation results on phase behavior of truncated cubes and hence allows the system to achieve equilibrium states.

Comparing our in situ transmission SAXS with the in situ GISAXS results by Weidman et al.[12], it is conceivable that the geometry of the cell (bulk-sensitive transmission SAXS vs. surface sensitive GISAXS), differences in solvent flow, and presence of cell walls (transmission SAXS) or the substrate (GISAXS) could play a role in the resulting assembly outcome. However, there are other factors that possibly influence the superlattice crystallization, such as e.g. slight differences in PbS nanocrystal size, shape and dispersity, different ligand grafting densities (which is a crucial parameter for the assembly of PbS NCs (see Ref. 42)), as well as different evaporation rates (and hence quasi equilibrium or out-of-equilibrium states). Further

experimental and theoretical investigations are required in order to precisely elucidate the origin of the observed experimental contradictions.

In summary, we carried out in situ SAXS measurements in transmission mode during the real-time evaporative assembly of faceted PbS NCs functionalized with oleic acid. This technique revealed different superlattice states compared to previously reported surface-sensitive GISAXS measurements. Using the XCCA approach, we were able to uncover the hidden Bragg reflections of the assembled structures and observed the coexistence of hcp and bct phases both in the solvated and dried superlattices. In this study, we demonstrated that the shape of the inorganic core dominates the assembly outcome of ligated NCs in the case of high ligand coverage and low softness of the NC core–ligand system as predicted by simulations. Thus, we confirmed our original hypothesis that self-assembly of colloidal nanocrystals located in the confined cell in our sample environment during the very slow and controlled solvent evaporation under the solvent vapor saturated atmosphere reaches thermodynamic equilibrium. The presented results provide valuable insights into the nucleation and growth of NC superlattices self-organized from faceted and ligated NCs.

ASSOCIATED CONTENT

Supporting Information. The Supporting Information is available free of charge.

Experimental methods, absorption spectrum of PbS NCs, thermogravimetric analysis of PbS NCs and calculation of ligand grafting density, calculation of the packing fraction of ligated nanocrystals, SAXS curves shown in Figure 2b with corresponding fits of the superlattice phases, time-resolved SAXS curves during in situ self-assembly of PbS NCs from toluene suspensions, WAXS patterns of PbS NCs in self-assembled superlattices (PDF).

AUTHOR INFORMATION

Corresponding Author

*E-mail: irina.lokteva@desy.de

Notes

The authors declare no competing financial interest.

ACKNOWLEDGMENTS

This work was funded by DESY, a member of the Helmholtz Association (HGF), and by the Clusters of Excellence 'The Hamburg Centre for Ultrafast Imaging' and 'Advanced Imaging of Matter' of the Deutsche Forschungsgemeinschaft (DFG), EXC 1074 – project ID 194651731 and EXC 2056 – project ID 390715994. The authors acknowledge the European Synchrotron Radiation Facility (ESRF), Grenoble, France for provision of synchrotron radiation facilities and thank Alessandro Mariani for assistance in using beamline ID02 (proposal SC-4605). Parts of this research were carried out at the University of Hamburg and at DESY NanoLab**.** The authors thank Andreas Kornowski for TEM and HRTEM images; Satishkumar Kulkarni for SEM images.

REFERENCES

(1) Si, K. J.; Chen, Y.; Shi, Q.; Cheng, W. Nanoparticle Superlattices: The Roles of Soft Ligands. *Adv. Sci.* **2018**, *5*, 1700179.

(2) Reichhelm, A.; Haubold, D.; Eychmüller, A. Ligand Versatility in Supercrystal Formation. *Adv. Funct. Mater.* **2017**, *27*, 1700361.

(3) Boles, M. A.; Engel, M.; Talapin, D. V. Self-Assembly of Colloidal Nanocrystals: From Intricate Structures to Functional Materials. *Chem. Rev.* **2016**, *116*, 11220–11289.

(4) Vogel, N.; Retsch, M.; Fustin, C.-A.; del Campo, A.; Jonas, U. Advances in Colloidal Assembly: The Design of Structure and Hierarchy in Two and Three Dimensions. Chem. Rev. **2015**, *115*, 6265–6311.

(5) Xu, L.; Ma, W.; Wang, L.; Xu, C.; Kuang, H.; Kotov, N. A. Nanoparticle Assemblies: Dimensional Transformation of Nanomaterials and Scalability. *Chem. Soc. Rev.* **2013**, *42*, 3114–3126.

(6) Hanrath, T. Colloidal Nanocrystal Quantum Dot Assemblies as Artificial Solids. *J. Vac. Sci. Technol. A* **2012**, *30*, 030802.

(7) Vanmaekelbergh, D. Self-Assembly of Colloidal Nanocrystals as Route to Novel Classes of Nanostructured Materials. *Nano Today* **2011**, *6*, 419–437.

(8) Damasceno, P. F.; Engel, M.; Glotzer, S. C. Predictive Self-Assembly of Polyhedra into Complex Structures. *Science* **2012**, *337*, 453–457.

(9) Henzie, J.; Grünwald, M.; Widmer-Cooper, A.; Geissler, P. L.; Yang, P. Self-Assembly of Uniform Polyhedral Silver Nanocrystals into Densest Packings and Exotic Superlattices. *Nat. Mater.* **2012**, *11*, 131–137.

(10) Yu, Y.; Yu, D.; Sadigh, B.; Orme, C. A. Space- and Time-Resolved Small Angle X-ray Scattering to Probe Assembly of Silver Nanocrystal Superlattices. *Nat. Commun.* **2018**, *9*, 4211.

(11) Maiti, S.; André, A.; Banerjee, R.; Hagenlocher, J.; Konovalov, O.; Schreiber, F.; Scheele, M. Monitoring Self-Assembly and Ligand Exchange of PbS Nanocrystal Superlattices at the Liquid/Air Interface in Real Time. *J. Phys. Chem. Lett.* **2018**, *9*, 739–744.

(12) Weidman, M. C.; Smilgies, D.-M.; Tisdale, W. A. Kinetics of the Self-Assembly of Nanocrystal Superlattices Measured by Real-Time *In Situ* X-ray Scattering. *Nat. Mater.* **2016**, *15*, 775–781.

(13) Josten, E.; Wetterskog, E.; Glavic, A.; Boesecke, P.; Feoktystov, A.; Brauweiler-Reuters, E.; Rücker, U.; Salazar-Alvarez, G.; Brückel, T.; Bergström, L. Superlattice Growth and Rearrangement during Evaporation-Induced Nanoparticle Self-Assembly. *Sci. Rep.* **2017**, *7*, 2802.

(14) Lu, C.; Akey, A. J.; Dahlman, C. J.; Zhang, D.; Herman, I. P. Resolving the Growth of 3D Colloidal Nanoparticle Superlattices by Real-Time Small-Angle X-ray Scattering. *J. Am. Chem. Soc.* **2012**, *134*, 18732–18738.

(15) Bian, K.; Choi, J. J.; Kaushik, A.; Clancy, P.; Smilgies, D.-M.; Hanrath, T. Shape-Anisotropy Driven Symmetry Transformations in Nanocrystal Superlattice Polymorphs. *ACS Nano* **2011**, *5*, 2815–2823.

(16) Cheng, W.; Hartman, M. R.; Smilgies, D.-M.; Long, R.; Campolongo, M. J.; Li, R.; Sekar, K.; Hui, C.-Y.; Luo, D. Probing in Real Time the Soft Crystallization of DNA-Capped Nanoparticles. *Angew. Chem. Int. Ed.* **2010**, *49*, 380–384.

(17) Li, T.; Senesi, A. J.; Lee, B. Small Angle X-ray Scattering for Nanoparticle Research. *Chem. Rev.* **2016**, *116*, 11128–11180.

(18) Huang, X.; Zhu, J.; Ge, B.; Deng, K.; Wu, X.; Xiao, T.; Jiang, T.; Quan, Z.; Cao, Y. C.; Wang, Z. Understanding Fe_3O_4 Nanocube Assembly with Reconstruction of a Consistent Superlattice Phase Diagram. *J. Am. Chem. Soc.* **2019**, *141*, 3198–3206.

(19) Yu, Y.; Guillaussier, A.; Voggu, V. R.; Houck, D. W.; Smilgies, D.-M.; Korgel, B. A.; Bubble Assemblies of Nanocrystals: Superlattices without a Substrate. *J. Phys. Chem. Lett.* **2017**, *8*, 4865–4871.

(20) Whitham, K.; Smilgies, D.-M.; Hanrath, T. Entropic, Enthalpic, and Kinetic Aspects of Interfacial Nanocrystal Superlattice Assembly and Attachment. *Chem. Mater.* **2018**, *30,* 54–63.

(21) Lokteva, I.; Walther, M.; Koof, M.; Grübel, G.; Lehmkühler, F. In Situ Small-Angle X-Ray Scattering Environment for Studying Nanocrystal Self-Assembly upon Controlled Solvent Evaporation. *Rev. Sci. Instrum.* **2019**, *90*, 036103.

(22) Lokteva, I.; Koof, M.; Walther, M.; Grübel, G.; Lehmkühler, F. Monitoring Nanocrystal Self-Assembly in Real Time Using In Situ Small-Angle X-Ray Scattering. *Small* **2019**, *15*, 1900438.

(23) Li, R.; Bian, K.; Hanrath, T.; Bassett, W. A.; Wang, Z. Decoding the Superlattice and Interface Structure of Truncate PbS Nanocrystal-Assembled Supercrystal and Associated Interaction Forces. *J. Am. Chem. Soc.* **2014**, *136*, 12047–12055.

(24) Hanrath, T.; Choi, J. J.; Smilgies, D.-M. Structure/Processing Relationships of Highly Ordered Lead Salt Nanocrystal Superlattices. *ACS Nano* **2009**, *3*, 2975–2988.

(25) Chen, W.; Zhong, J.; Li, J.; Saxena, N.; Kreuzer, L. P.; Liu, H.; Song, L.; Su, B.; Yang, D.; Wang, K. et al. Structure and Charge Carrier Dynamics in Colloidal PbS Quantum Dot Solids. *J. Phys. Chem. Lett.* **2019**, *10*, 2058–2065.

(26) Bian, K.; Li, R.; Fan, H. Controlled Self-Assembly and Tuning of Large PbS Nanoparticle Supercrystals. *Chem. Mater.* **2018**, *30*, 6788–6793.

(27) Rupich, S. M.; Shevchenko, E. V.; Bodnarchuk, M. I.; Lee, B.; Talapin, D. V. Size-Dependent Multiple Twinning in Nanocrystal Superlattices. *J. Am. Chem. Soc.* **2010,** *132*, 289–296.

(28) Diroll, B. T.; Ma, X.; Wu, Y.; Murray, C. B. Anisotropic Cracking of Nanocrystal Superlattices. *Nano Lett.* **2017**, *17*, 6501–6506.

(29) Simon, P.; Rosseeva, E.; Baburin, I. A.; Liebscher, L.; Hickey, S. G.; Cardoso-Gil, R.; Eychmüller, A.; Kniep, R.; Carrillo-Cabrera, W. PbS–Organic Mesocrystals: The Relationship between Nanocrystal Orientation and Superlattice Array. *Angew. Chem. Int. Ed.* **2012**, *51*, 10776–10781.

(30) Goodfellow, B. W.; Yu, Y.; Bosoy, C. A.; Smilgies, D.-M.; Korgel, B. A. The Role of Ligand Packing Frustration in Body-Centered Cubic (bcc) Superlattices of Colloidal Nanocrystals. *J. Phys. Chem. Lett.* **2015**, *6*, 2406–2412.

(31) Weidman, M. C.; Yager, K. G.; Tisdale, W. A. Interparticle Spacing and Structural Ordering in Superlattice PbS Nanocrystal Solids Undergoing Ligand Exchange. *Chem. Mater.* **2015**, *27*, 474–482.

(32) Quan, Z.; Loc, W. S.; Lin, C.; Luo, Z.; Yang, K.; Wang, Y.; Wang, H.; Wang, Z.; Fang, J. Tilted Face-Centered-Cubic Supercrystals of PbS Nanocubes. *Nano Lett.* **2012**, *12*, 4409–4413.

(33) Bian, K.; Wang, Z.; Hanrath, T. Comparing the Structural Stability of PbS Nanocrystals Assembled in fcc and bcc Superlattice Allotropes. *J. Am. Chem. Soc.* **2012**, *134*, 10787–10790.

(34) Wang, Z.; Schliehe, C.; Bian, K.; Dale, D.; Bassett, W. A.; Hanrath, T.; Klinke, C.; Weller, H. Correlating Superlattice Polymorphs to Internanoparticle Distance, Packing Density, and Surface Lattice in Assemblies of PbS Nanoparticles. *Nano Lett.* **2013**, *13*, 1303–1311.

(35) Novák, J.; Banerjee, R.; Kornowski, A.; Jankowski, M.; André, A.; Weller, H.; Schreiber, F.; Scheele, M. Site-Specific Ligand Interactions Favor the Tetragonal Distortion of PbS Nanocrystal Superlattices. *ACS Appl. Mater. Interfaces* **2016**, *8*, 22526–22533.

(36) Zaluzhnyy, I. A.; Kurta, R. P.; André, A.; Gorobtsov, O. Y.; Rose, M.; Skopintsev, P.; Besedin, I.; Zozulya, A. V.; Sprung, M.; Schreiber, F.; Vartanyants, I. A.; Scheele, M. Quantifying Angular Correlations between the Atomic Lattice and the Superlattice of Nanocrystals Assembled with Directional Linking. *Nano Lett.* **2017**, *17*, 3511–3517.

(37) Weidman, M. C.; Nguyen, Q.; Smilgies, D.-M., Tisdale, W. A. Impact of Size Dispersity, Ligand Coverage, and Ligand Length on the Structure of PbS Nanocrystal Superlattices. *Chem. Mater.* **2018**, *30*, 807–816.

(38) Wang, Z.; Bian, K.; Nagaoka, Y.; Fan, H.; Cao, Y.C. Regulating Multiple Variables to Understand the Nucleation and Growth and Transformation of PbS Nanocrystal Superlattices. *J. Am. Chem. Soc.* **2017**, *139*, 14476–14482.

(39) Bealing, C.R.; Baumgardner, W.J.; Choi, J.J.; Hanrath, T.; Hennig, R.G. Predicting Nanocrystal Shape through Consideration of Surface-Ligand Interactions. *ACS Nano* **2012**, *6*, 2118–2127.

(40) Travesset, A. Soft Skyrmions, Spontaneous Valence and Selection Rules in Nanoparticle Superlattices. *ACS Nano* **2017**, *11*, 5375–5382.

(41) Travesset, A. Topological Structure Prediction in Binary Nanoparticle Superlattices. *Soft Matter* **2017**, *13*, 147–157.

(42) Boles, M. A.; Talapin, D. V. Binary Assembly of PbS and Au Nanocrystals: Patchy PbS Surface Ligand Coverage Stabilizes the CuAu Superlattice. *ACS Nano* **2019**, *13*, 5375–5384.

(43) Narayanan, T.; Diat, O.; Bösecke, P. SAXS and USAXS on the high brilliance beamline at the ESRF. *Nucl. Instrum. Meth. A.* **2001**, *467*, 1005–1009.

(44) Narayanan, T.; Sztucki, M.; Van Vaerenbergh, P.; Léonardon, J.; Gorini, J.; Claustre, L.; Sever, F.; Morse, J.; Boesecke, P. A Multipurpose Instrument for Time-Resolved Ultra-Small-Angle and Coherent X-ray Scattering. J. Appl. Cryst. **2018**, *51*, 1511–1524.

(45) Salentinig, S.; Sagalowicz, L.; Glatter. O. Self-Assembled Structures and pKa Value of Oleic Acid in Systems of Biological Relevance. *Langmuir* **2010**, *26*, 11670–11679.

(46) Rosenfeldt, S.; Förster, S.; Friedrich, T.; Rehberg, I.; Weber, B. In *Novel Magnetic Nanostructures*; Elsevier Inc., 2018; pp 165–189.

(47) Liepold, C.; Smith, A.; Lin, B.; de Pablo, J.; Rice, S. A. Pair and Many-Body Interactions Between Ligated Au Nanoparticles. *J. Chem. Phys*. **2019**, *150*, 044904.

(48) Patra, T. K.; Chan, H.; Podsiadlo, P.; Shevchenko, E. V.; Sankaranarayanan, S. K. R. S.; Narayanan, B. Ligand Dynamics Control Structure, Elasticity, and High-Pressure Behavior of Nanoparticle Superlattices. *Nanoscale* **2019**, *11*, 10655–10666.

(49) Wochner, P.; Gutt, C.; Autenrieth, T.; Demmer, T.; Bugaev, V.; Díaz Ortiz, A.; Duri, A.; Zontone, F.; Grübel, G.; Dosch, H. X-ray Cross Correlation Analysis Uncovers Hidden Local Symmetries in Disordered Matter. *Proc. Natl. Acad. Sci. U.S.A* **2009**, *106*, 11511–11514.

(50) Kurta, R. P.; Altarelli, M.; Vartanyants, I. A. In *Advances in Chemical Physics*; John Wiley & Sons, Inc., 2016; pp 1–39.

(51) Lehmkühler, F.; Fischer, B.; Müller, L.; Ruta, B.; Grübel, G. Structure beyond Pair Correlations: X-ray Cross-Correlation from Colloidal Crystals. *J. Appl. Cryst.* **2016**, *49*, 2046–2052.

(52) Mendez, D.; Watkins, H.; Qiao, S.; Raines, K. S.; Lane, T. J.; Schenk, G.; Nelson, G.; Subramanian, G.; Tono, K.; Joti, Y.; Yabashi, M.; Ratner, D.; Doniach, S. Angular Correlations of Photons from Solution Diffraction at a Free-Electron Laser Encode Molecular Structure. *IUCrJ* **2016**, *3*, 420–429.

(53) Lehmkühler, F.; Schulz, F.; Schroer, M. A.; Frenzel, L.; Lange, H.; Grübel, G. Heterogeneous Local Order in Self-Assembled Nanoparticle Films Revealed by X-ray Cross-Correlations. *IUCrJ* **2018**, *5*, 354–360.

(54) Lehmkühler, F.; Schulz, F.; Schroer, M.; Frenzel, L.; Lange, H.; Grübel, G. Local Orientational Order in Self-Assembled Nanoparticle Films: the Role of Ligand Composition and Salt. *J. Appl. Cryst.* **2019**, *52*, 777–782.

(55) Mendez, D.; Lane, T. J.; Sung, J.; Sellberg, J.; Levard, C.; Watkins, H.; Cohen, A. E.; Soltis, M.; Sutton, S.; Spudich, J.; Pande, V.; Ratner, D.; and Doniach, S. Observation of Correlated X-ray Scattering at Atomic Resolution. *Phil. Trans. R. Soc. B.* **2014**, *369*, 20130315.

(56) Lehmkühler, F.; Grübel , G.; Gutt, C. Detecting Orientational Order in Model Systems by X-ray Cross-Correlation Methods. *J. Appl. Cryst.* **2014**, *47*, 1315–1323.

(57) Vester, P.; Zaluzhnyy, I. A.; Kurta, R. P.; Møller, K. B.; Biasin E.; Haldrup, K.;, Nielsen, M. M.; Vartanyants, I. A. Ultrafast Structural Dynamics of Photo-Reactions Observed by Time-Resolved X-ray Cross-Correlation Analysis. *Struct. Dyn.* **2019**, *6*, 024301.

(58) Kaushik, A. P.; Clancy, P. Solvent-Driven Symmetry of Self-Assembled Nanocrystal Superlattices – A Computational Study. *J. Comput. Chem.* **2013**, *34*, 523–532.

(59) Gantapara, A. P.; de Graaf, J.; van Roij, R.; Dijkstra, M. Phase Diagram and Structural Diversity of a Family of Truncated Cubes: Degenerate Close-Packed Structures and Vacancy-Rich States. *Phys. Rev. Lett.* **2013**, *111*, 015501.

(60) Gantapara, A. P.; de Graaf, J.; van Roij, R.; Dijkstra, M. Phase Behavior of a Family of Truncated Hard Cubes. *J. Chem. Phys.* **2015**, *142*, 054904.